Non-unit wavelet transform-based protection principle for modular multi-level converter-based HVDC grids using adaptive threshold setting

Dehghan Marvasti, Farzad; Mirzaei, Ahmad; Bakhshi-Jafarabadi, Reza; Popov, Marjan

DOI
10.1016/j.ijepes.2024.110352

Publication date
2024

Document Version
Final published version

Published in
International Journal of Electrical Power and Energy Systems

Electrical Power and Energy Systems 163 (2024) 110352

Contents lists available at ScienceDirect

International Journal of Electrical Power and Energy Systems

journal homepage: www.elsevier.com/locate/ijepes

Non-unit wavelet transform-based protection principle for modular multi-level converter-based HVDC grids using adaptive threshold setting

Farzad Dehghan Marvasti [a,b,*], Ahmad Mirzaei [b], Reza Bakhshi-Jafarabadi [a], Marjan Popov [a]

[a] Delft University of Technology, Faculty of EEMCS, Mekelweg 4, Delft 2628CD, the Netherlands
[b] Department of Electrical Engineering, Yazd University, Yazd, Iran

ARTICLE INFO

Keywords:
Adaptive threshold
MMC-based HVDC grid
Traveling wave-based protection
Wavelet transform

ABSTRACT

Wavelet transform has proven to be a capable tool for protection purposes in high voltage direct current (HVDC) transmission lines due to its desired speed and accuracy. However, the need to enhance the WT-based protection methods in terms of sensitivity and selectivity is of interest. This paper proposes a new non-unit WT-based protection method with adaptive threshold setting. According to the improved time-domain analytical approach, line-mode fault-generated voltage traveling wave is adopted to identify the internal faults. The simulation results for a multi-terminal modular multilevel converter-based HVDC grid in PSCAD/EMTDC corroborate accurate and fast internal faults detection of the proposed method, up to 850 Ω, i.e., almost three times larger than conventional schemes. In addition, the reliable performance of the presented method in a noisy environment, using relatively low sampling frequencies, and different sizes of current limiting inductors is demonstrated in the presented analysis. The generality of the presented analytical approach ensures that the proposed protection method can be extended to more complex HVDC grids.

1. Introduction

Large-scale integration of renewable energy resources increases steadily due to the economic-benefit goals of green energy generation. To this end, high voltage direct current (HVDC) grids incorporating modular multilevel converters (MMC), with several advantages such as independent active and reactive power control, robustness to disturbances, and power reverse capability, are widely used [1,2]. Despite the advantages, MMC-based HVDC systems require fast protective measures to deal with the devastating DC fault currents that can quickly damage the power electronic devices inside the converters [3]. In addition, the employed protection method should disconnect only the faulty lines under DC faults. Hence, this selectivity feature is an important factor for the reliable operation of multi-terminal HVDC systems. In the development of multi-terminal HVDC systems, a comprehensive DC fault analysis and fault identification that leads to the design of a fast and selective protection principle is still challenging.

1.1. Background of HVDC protection principles

At present, the protection of conventional HVDC transmission lines is relatively mature. Traditional traveling wave (TW)-based and undervoltage protection principles are used as the primary protection, and current differential protection as the backup solution [4–6]. However, as fault resistance increases, the amplitudes of the traveling-waves attenuate, degrading the performance of the traditional TW-based and undervoltage protection methods under faults with higher resistances. To improve the performance of the traditional primary protection schemes, advanced transient-based methods have been developed in various studies, e.g., voltage across the current limiting inductor (CLI) [7] and CLI power [8]. Although these methods have sufficiently supported high speed and sensitivity, they cannot identify DC faults with higher resistances [9,10]. Employing multi-resolution morphological gradient algorithm and equivalent capacitance voltage of MMCs, non-unit protection schemes based on distance criteria are introduced in [11,12]. These methods can be effectively adopted as supplement protections to transient-based methods.

Advanced TW-based methods are other promising primary protective solutions with fast response and accuracy. A setting-less non-unit protection method has been introduced in [13]. This method uses curve fitting and the Levenberg-Marquardt optimal approximation to distinguish between internal and external faults. As a non-unit ultra-high-

* Corresponding author at: Delft University of Technology, Faculty of EEMCS, Mekelweg 4, Delft 2628CD, the Netherlands.
E-mail address: F.DehghanMarvasti@TUDelft.nl (F. Dehghan Marvasti).

https://doi.org/10.1016/j.ijepes.2024.110352
Received 25 March 2024; Received in revised form 28 August 2024; Accepted 29 October 2024
Available online 13 November 2024

speed protection, the first peak time of the line-mode fault-component voltage TW has been adopted in [14] to identify internal faults. Despite overall outstanding performance, this work requires a high sampling frequency. Focusing on the frequency-domain characteristics and polarity of TWs, an ultra-high-speed protection scheme has been presented in [15]. Although it relies solely on the initial fault-generated TW, the requirement for high sampling frequency limits its implementation [15]. To distinguish high-resistance internal faults from severe external faults, a method to investigate a distinct current reduction phenomenon between two fault-generated TWs is proposed in [16]. However, this method cannot cover the whole length of the transmission line under specific faults. A voltage TW differential protection method with immunity to out-of-sync data and lightning disturbance has been presented in [17]. Ref. [18] developed a hybrid derivative/TW protection method, by employing an adaptive threshold value to improve the performance of its voltage derivative criterion.

When it comes to pilot protection methods, recent studies have improved the application of the current differential protection scheme with greater robustness against either the detrimental effect of the distributed capacitance of transmission line [19,20] or the negative impact of transmission line parameter's error [21]. Other variants of the pilot protection methods based on directional criteria have been proposed in [22,23]. While [22] employs the fault signature arrival time difference of line-mode backward and forward TWs as a direction criterion, an improved version of the traditional transient TW-based direction criterion that is independent of the line boundary is used in [23]. The energy ratio and comparison between the forward and backward fault-generated TWs have been exploited in [24,25] for DC fault protection. However, the performance of these methods degrades for fault scenarios with higher resistance.

1.2. Related works and main Contributions

Wavelet transform (WT) has shown promising performance in the protection of MMC-based HVDC grids. Among the WT-based protection studies, [26] presented a not-unit analytical protection scheme, where the impact of various mother wavelets and wavelet decomposition scales on its performance has been investigated. In [27], a WT-based protection method with a low computational burden has been adopted. However, both methods are vulnerable to environmental noise.

Based on the polarity of current TWs, a WT-based protection scheme has been suggested in [28], which detects internal faults up to 300 Ω. However, being a pilot protection method, the fault identification speed of this method is generally lower than similar primary WT-based schemes. Frequency-domain protection solutions that use WT to extract high-frequency components of voltage TW are presented in [29–31]. Despite the fast and precise performance, these works heavily rely on simulation studies to properly set their protective thresholds. A high sampling frequency of 500 kHz for reliable operation is another shortcoming of the presented method in [31]. Wavelet transform modulus maximum (WTMM) associated with line-mode backward voltage traveling-wave has been applied for fault identification [32]. The method has shown good performance; however, it suffers from a high sampling frequency of 1 MHz and a large computational burden. Furthermore, the presented methods in [26–33] are effective in identifying internal faults up to a certain impedance (commonly around 350 Ω), after which the selectivity of these protection methods declines.

Based on the literature, there are several WT-based methods for primary control of MMC-based multi-terminal HVDC grids. However, the development of a new accurate, and fast methodology with low complexity, and low sampling frequency that covers a wide range of fault resistances is of interest. In this perspective, this paper proposes a non-unit WT-based protection principle with an adaptive threshold setting. A comprehensive analytical time-domain approach supports the proposed method to ensure its performance and validity. In comparison to the existing solutions, this paper provides the following advantages:

- Improved analytical calculation of fault-generated waveforms via accurate modeling of the modal wave impedances and propagation function, ensuring a robust protective threshold determination and general adaptability of the proposed protection principle to any system configuration.
- Enhanced selectivity in fault identification up to 850 Ω through employing adaptive threshold.
- Inherent discrimination of forward and backward faults, eliminating the need for a dedicated directional criterion.
- Maintaining solid performance in a noisy environment and low CLI size.

The rest of the paper is organized as follows. The analytical extraction of line-mode fault-generated voltage TW (LFVTW) is presented in Section 2. The procedure to improve WT-based protection is demonstrated in Section 3. The proposed protection method and its components are presented in Section 4. Section 5 evaluates the performance of the proposed method under various fault scenarios. Finally, Section 6concludes the paper.

2. Design of wavelet transform-based methodology

The proposed protection method is based on an analytical approach. In this section, an MMC-based multiterminal HVDC grid is introduced and the analytical expressions are then described. For this purpose, a four-terminal ± 500 kV MMC HVDC transmission grid simulated in the PSCAD/EMTDC platform with the schematic diagram and parameters respectively presented in Fig. 1 and Table 1, is considered.

The T_1-T_4 DC terminals are interconnected via four 400-km bipolar overhead transmission lines, modeled with frequency-dependent line parameters. The CLIs are employed to lower the requirement for DC protection [3]. Measurement units and protective relays are installed at both ends of each line indicated by R_1-R_4 and R'_1-R'_4. Internal and external faults at various locations (f_1-f_5) include pole-to-pole (PTP) and single-pole-to-ground (SPG) faults. Note that SPG faults are positive-pole-to-ground (PTG) and negative-pole-to-ground (NTG) faults.

The proposed analytical representation of LFVTW provides a general procedure for threshold determination, useful to a wide range of existing WT and TW-based primary protection methods that have exploited the

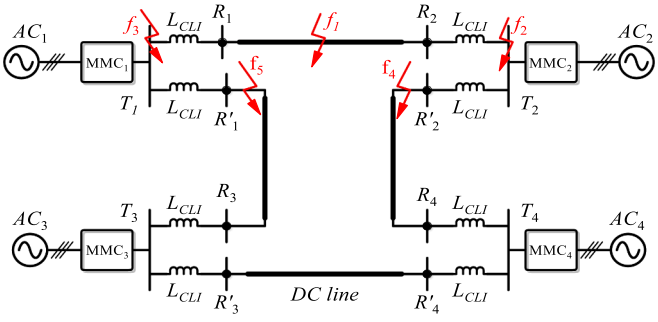

Fig. 1. Schematic diagram of MMC-HVDC test grid.

Table 1
Parameters of MMC-HVDC test grid.

System parameters	MMC1 ~ MMC4
Rated power	2000 MW
Rated DC voltage,U_{dc}	± 500 kV
Rated AC voltage	400 kV
Transformer ratio	400 kV/300 kV
Transformer leakage reactance	0.15 pu
CLI	100 mH
Converter arm inductor	40 mH
Number of submodules per arm	225
Submodule capacitance	9000 μ F

time-domain DC pole voltage or LFVTW. This analytical approach should ensure that all important factors and system non-linearities affecting the fault-generated TWs are properly considered. Therefore, the detailed equivalent circuit model of the converter (type-4) and the frequency-dependent model of the transmission lines are used [34]. The analytical approach is derived for the protection system installed at terminal R_1 in Fig. 1. Regardless of the fault location, the time-domain derivation of LFVTW at R_1 includes the following four consecutive steps:

1. Extraction of LFVTW at the fault location,
2. Determination of LFVTW at R_1,
3. Vector fitting (VF) employment to represent the frequency-dependent characteristics of the modal propagation function and wave impedances,
4. Applying inverse Laplace transform to extract the time-domain response.

This process is examined for three scenarios, internal faults, forward external faults, and reverse external faults, described as follows. Obviously, for the other DC terminals of the grid, a similar approach can be taken. The analytical approach is conducted for a single transmission line of the 4-terminal HVDC test grid, which is considered as an effective smaller-scale representation of more complex HVDC grids. By extending this approach to additional transmission lines, a comprehensive protection method for larger HVDC grids can be developed. Therefore, the generality of the proposed analytical approach is ensured.

2.1. Time-domain derivation of LFVTW under internal faults

The analytical approach under internal faults is elaborated based on the equivalent line-mode circuit of the MMC-based HVDC grid from the fault location to terminal R_1 (Fig. 2).

As an example for a PTG fault, the modal components of the pole voltages can be extracted via the decoupling process performed by (1), which resolves the positive and negative pole voltages (u_p and u_n) into their equivalent zero-mode and line-mode components (u_0 and u_1).

$$\begin{bmatrix} u_0 \\ u_1 \end{bmatrix} = \frac{1}{\sqrt{2}} \begin{bmatrix} 1 & 1 \\ 1 & -1 \end{bmatrix} \begin{bmatrix} u_p \\ u_n \end{bmatrix} \tag{1}$$

After the decoupling process, the zero- and line-mode voltage variations ($\Delta u_{flt,0}$ and $\Delta u_{flt,1}$) at fault location are derived. These components can be presented by Eqs. (2)–(4) for PTG, NTG, and PTP faults, respectively [35]:

$$\Delta u_{flt,0} = \frac{-\sqrt{2}U_{dc}.Z_0}{s(Z_0+Z_1+2R_f)}, \Delta u_{flt,1} = \frac{-\sqrt{2}U_{dc}.Z_1}{s(Z_0+Z_1+2R_f)} \tag{2}$$

$$\Delta u_{flt,0} = \frac{\sqrt{2}U_{dc}.Z_0}{s(Z_0+Z_1+2R_f)}, \Delta u_{flt,1} = \frac{-\sqrt{2}U_{dc}.Z_1}{s(Z_0+Z_1+2R_f)} \tag{3}$$

$$\Delta u_{flt,0} = 0 \ , \ \Delta u_{flt,1} = \frac{-2\sqrt{2}U_{dc}.Z_1}{s(2Z_1+R_f)} \tag{4}$$

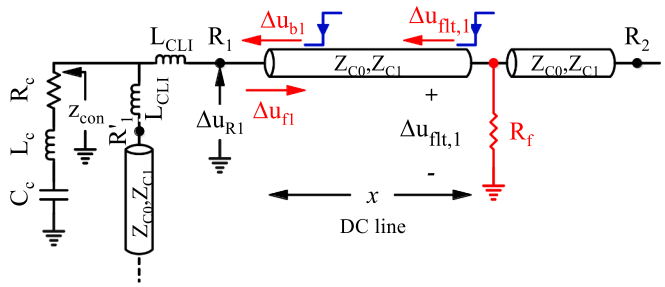

Fig. 2. Process of LFVTW calculation at R_1 under internal faults.

where U_{dc} is the rated DC pole voltage, and R_f is the fault resistance. Also, Z_0 and Z_1 are the Thevenin-equivalent zero- and line-mode impedances observed from the fault point, respectively. These impedances are computed as follows:

$$Z_0 = Z_{c0}/2, \quad Z_1 = Z_{c1}/2 \tag{5}$$

where Z_{c0} and Z_{c1} are the zero- and line-mode wave impedances, respectively. Following the extraction of the LFVTW waveform at the fault location, the expression at R_1 should be obtained. After the fault occurrence, LFVTW at the fault location propagates along the transmission line and is consequently distorted by the propagation function, as shown in Fig. 2. When the LFVTW hits the line boundary at R_1, it is partially reflected to the transmission line. Therefore, LFVTW at R_1 (Δu_{R1}) is the superposition of the fault voltage incident TW; the backward component (Δu_{b1}) and its reflected forward wave (Δu_{f1}). These components can be expressed as follows:

$$\Delta u_{R1} = \Delta u_{b1} + \Delta u_{f1} = \Delta u_{flt,1}.e^{-\gamma_1(s)x} + \Gamma_1.\Delta u_{flt,1}.e^{-\gamma_1(s)x} \tag{6}$$

$$\Gamma_1 = \frac{Z_{con}\|(sL_{CLI}+Z_{c1}) + sL_{CLI} - Z_{c1}}{Z_{con}\|(sL_{CLI}+Z_{c1}) + sL_{CLI} + Z_{c1}} \tag{7}$$

$$Z_{con} = R_c + sL_c + \frac{1}{sC_c} \tag{8}$$

where Γ_1, γ_1, and x are the line-mode reflection coefficient, line-mode propagation function, and fault location, respectively. Also, Z_{con} represents the converter impedance via an equivalent series RLC circuit [3]. Moreover, $R_c = 2(R_{arm}+R_{on})/3$, $L_c = 2L_{arm}/3$, and $C_c = 6C_{sm}/N$, where R_{arm}, L_{arm}, C_{sm}, and N are the arm resistance, the arm inductance, the capacitance of the inserted sub-modules, and the total number of inserted sub-modules, respectively. Finally, R_{on} is the on-state resistance of the entire inserted sub-modules in each converter arm.

Line-mode propagation coefficient, γ_1 (s) in (9) and modal wave impedances, Z_{c0} and Z_{c1} in (10), are frequency-dependent in nature.

$$\gamma_i(s) = \sqrt{(r_i(s)+jwL(s)_i).(g_i+jwC_i(s))} \tag{9}$$

$$Z_{ci}(s) = \sqrt{(r_i(s)+jwL_i(s))/(g_i+jwC_i(s))} \tag{10}$$

where r_i, L_i, g_i, and C_i ($i = 0$ and 1) are the zero/line-mode resistance, inductance, conductance, and capacitance per unit length of the transmission line, respectively. This frequency dependency is evident in Fig. 3 (a) and (b), where the magnitudes of the modal propagation functions ($e^{-\gamma_i(s)x}$) and modal wave impedances (Z_{ci}(s)) are depicted, respectively. Using Eqs. (9) and (10), the line-mode propagation function, $e^{-\gamma_1(s)x}$ and modal wave impedances will be complex quantities. Therefore, VF with a non-linear rational approximation is used to model $e^{-\gamma_1(s)x}$, Z_{c0}(s), and Z_{c1}(s) to properly incorporate them into Eqs. (5), (6) and (7), and have a

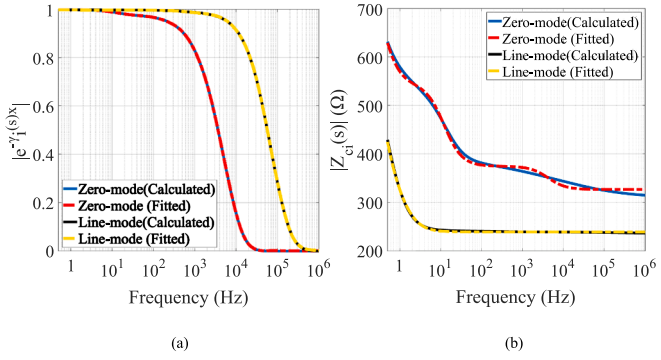

Fig. 3. Frequency characteristic of: (a) modal propagation functions; and (b) modal wave impedances.

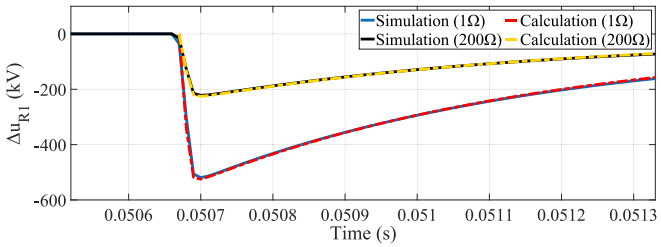

Fig. 4. Comparison between analytical and simulation results of LFVTW under various internal faults.

precise frequency-domain representation of LFVTW [36]. These quantities are expressed as follows:

$$e^{-\gamma_1(s)x} \cong F_e(s) = \sum_{k=1}^{n} \frac{C_k}{s - A_k} + D \tag{11}$$

$$Z_{c0}(s) \cong F_{c0}(s) = \sum_{k=1}^{n} \frac{C_k}{s - A_k} + D \tag{12}$$

$$Z_{c1}(s) \cong F_{c1}(s) = \sum_{k=1}^{n} \frac{C_k}{s - A_k} + D, \tag{13}$$

where C_k and A_k are complex residues and poles, respectively, and D is a real constant. A comparison between the calculated and fitted versions of the line-mode propagation function and zero- and line-mode wave impedances are presented in Fig. 3(a) and (b), respectively. As the significance of accurate fitting will be discussed later, the presented results corroborate the accurate estimation of these impedances. Afterward, the frequency-domain expression of LFVTW at R_1 can be deducted from Eqs. (2)–(13) with the following general form:

$$\Delta u_{R1} = \Delta u_{b1} + \Delta u_{f1} = (1 + \Gamma_1).\Delta u_{flt,1}.F_e(s) \tag{14}$$

Finally, the time-domain expression of LFVTW can be derived by applying the inverse Laplace transform to (14) after substituting the variable with related system quantities. Fig. 4 demonstrates the accuracy of the analytical approach, where the computed outputs are compared with the simulation results of LFVTW from the simulated test system. It is worth mentioning that the faults happen at 200 km with 1 Ω and 200 Ω resistances.

2.2. Time-domain derivation of LFVTW under forward external faults

Similar to the internal faults, the four-step procedure is realized to extract the analytical expression of LFVTW under forward external faults. This procedure is demonstrated based on Fig. 5.

The expression of LFVTW at the fault location ($\Delta u_{flt,1}$) is firstly extracted by expressions (2)–(4) in which Z_0 and Z_1 can be obtained as:

$$\begin{cases} Z_0 = (sL_{CLI} + Z_{c0}) \| (Z_{con} \| (sL_{CLI} + Z_{c0})), \\ Z_1 = (sL_{CLI} + Z_{c1}) \| (Z_{con} \| (sL_{CLI} + Z_{c1})). \end{cases} \tag{15}$$

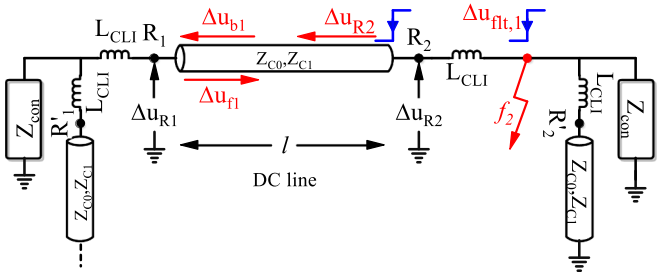

Fig. 5. Process of LFVTW calculation at R_1 under forward external faults.

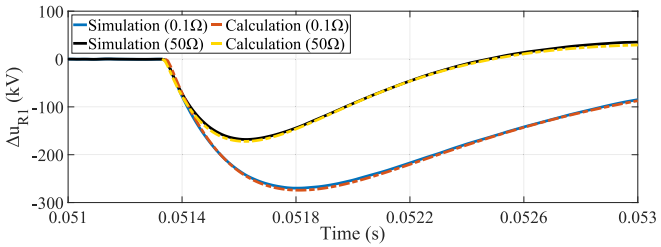

Fig. 6. Comparison between analytical and simulation results of LFVTW under various forward external faults.

Before calculating the LFVTW at R_1, LFVTW at the remote-end terminal (R_2) is computed by (16). This equation demonstrates the impact of CLI on the LFVTW by Λ_1.

$$\begin{cases} \Delta u_{R2} = \Delta u_{flt,1}.\Lambda_1 \\ \Lambda_1 = \dfrac{Z_{c1}}{Z_{c1} + sL_{CLI}} \end{cases} \tag{16}$$

After propagating through the transmission line and reaching the line boundary at the local terminal R_1, the expression of LFVTW in the frequency domain can be presented as:

$$\Delta u_{R1} = \Delta u_{b1} + \Delta u_{f1} = (1 + \Gamma_1).\Delta u_{flt,1}.\Lambda_1.F_{el}(s) \tag{17}$$

where Γ_1 and Z_{c0} are expressed by (7) and (12), respectively. Furthermore, F_{el}(s) represents the line-mode propagation function calculated by (11) for $x = l$. Finally, the time-domain response of the LFVTW can be determined by applying the inverse Laplace transform to (17). The comparison of analytical results with simulation results of LFVTW, when forward external faults with 1 Ω and 50 Ω occur, is shown in Fig. 6.

2.3. Time-domain derivation of LFVTW under reverse external faults

The expression of LFVTW at R_1 under reverse external faults is identical to the forward external faults at R_2. In the latter case, LFVTW consists of a forward wave component, as can be observed in Fig. 7. Therefore, LFVTW at R_1 can be expressed as:

$$\Delta u_{R1} = \Delta u_{f1} = \Delta u_{flt,1}.\frac{Z_{c1}}{Z_{c1} + sL_{CLI}} \tag{18}$$

where Δu_{flt1} is indicated by (2)–(4), in which Z_0 and Z_1 are defined by (15). After taking the inverse Laplace transform of (18), the time-domain response can be derived. To determine the accuracy of the analytical approach, a comparison to simulation results under reverse external faults with 1 Ω and 50 Ω is depicted in Fig. 8.

Based on the outputs of the presented expressions and simulation, the proposed new analytical approach effectively analyzes the characteristics of TWs in the modal domain during various types of internal and external faults. Furthermore, it is a robust way of determining the

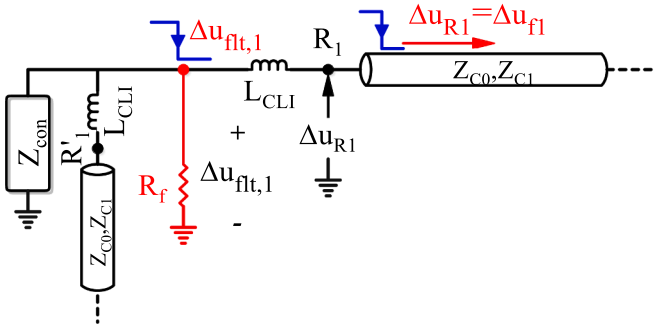

Fig. 7. Process of LFVTW calculation at R_1 under reverse external faults.

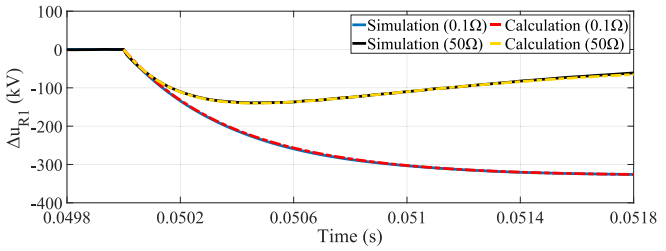

Fig. 8. Comparison between analytical and simulation results of LFVTW under various reverse external faults.

protective threshold under any system configuration. Moreover, although WT-based protection methods are the focus of this study, the presented analytical approach can be employed for any TW-based protection principle. Thus, it can be considered as a general approach.

2.4. Importance of accuracy in analytical investigations for application of wavelet transform

This paper adopts the WT on LFVTW to extract WTMM for fault detection, as will be discussed in the following section. The WTMM results are primarily influenced by the abrupt changes in LFVTW during various DC faults. The accuracy of the analytical investigations in modeling LFVTW, especially during the initial period of TWs reaching the DC terminals, is essential. Any modeling inaccuracies during this time frame can significantly affect the WTMM results.

Most existing studies have simplified the modeling of LFVTW, resulting in inaccuracies. The simplifications typically relate to the frequency-dependent characteristics of zero- and line-mode wave impedances, and line-mode propagation function. In the simplified model, for example, the propagation function is determined as follows [13,14]:

$$e^{-\gamma_1(s)x} \approx \frac{1-k_{a1}x}{1+s\tau_{a1}x}e^{-sT} \tag{19}$$

where e^{-sT} is the delay caused by the transmission line. Also, k_{a1} and τ_{a1} are the line-mode attenuation coefficient and dispersion time constant of the DC transmission, respectively. As shown in Fig. 3-b, these impedances are frequency-dependent and can affect the LFVTW characteristics. This effect on the WTMM during internal faults is demonstrated by a few analysis. A comparison of LFVTW and the resulted WTMM between the simulation results, the simplified modeling, and the proposed comprehensive approach is illustrated in Fig. 9. The case represents a 1 Ω internal fault at 300 km, and the sampling frequency is 20 kHz.

Despite the apparent similarity of the waveforms in Fig. 9, their WTMMs show noticeable deviations, affecting the performance of WT-based protection principles. In contrast, a comprehensive approach is considered in this paper by incorporating the complete representation of the zero- and line-mode wave impedances and the propagation function using Eqs. (11)–(13). These equations are complex algebraic formulas with several terms, and their use in modeling can significantly increase the computational burden during the inverse Laplace transformation.

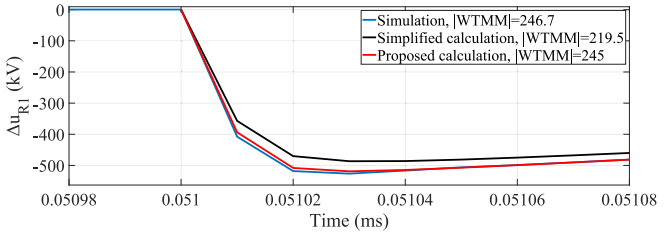

Fig. 9. A Comparison of LFVTW Results at R_1: Simulation vs. simplified calculations vs. proposed calculations.

Accordingly, finding a trade-off between accuracy and the level of complexity is crucial. In this regard, an error tolerance of −30 dB is considered for the line-mode wave impedance and propagation function. Also, an error tolerance of −40 dB is set for the zero-mode wave impedance for the VF procedure. Hereby, the line-mode wave impedance and propagation function are modelled by five terms in Eqs. (11) and (13), respectively, while the zero-mode wave impedance has been presented by seven terms in (12).

3. Design consideration of proposed wavelet transfer-based protection principle

3.1. Application of wavelet transform in HVDC protection

Based on the presented analysis in Figs. 4, 6, and 8, it can be concluded that the severity of the voltage drop rate under the internal faults is significantly higher than that under the external faults. This phenomenon is mainly related to the impact of CLI during external faults and suppressing the high-frequency components of the TWs. These high-frequency components are typically in the range of 3–10 kHz and can be used in the discrimination of internal and external faults [26,27,32]. Due to its convenient function in time and frequency localization, WT can be used to extract these high-frequency components in a specific frequency spectrum, making it an attractive tool for protective purposes. In this regard, discrete wavelet transform (DWT) is a computationally effective and widely employed method of analyzing TWs, in which multiresolution signal decomposition is applied through a series of low-pass and high-pass filtering processes. However, information loss is one major disadvantage of DWT in high-frequency bands due to the down-sampling process inherent to each decomposition implementation [37]. Despite having a small deficiency in calculations, stationary wavelet transform (SWT) is accordingly employed to avoid this issue and consistently extract the high-frequency components. The approximation and detail coefficients at level j, namely $a_j(k)$ and $d_j(k)$, using SWT can be obtained as follows:

$$\begin{cases} a_j(k) = \sum_n a_{j-1}(n)h_0(n-2k) \\ d_j(k) = \sum_n a_{j-1}(n)h_1(n-2k) \end{cases} \tag{20}$$

here the low-pass and high-pass filter arrays are denoted by h_0 and h_1, respectively.

Due to stronger high-frequency components under internal faults, the maximum absolute value of the WT results (hereafter referred to as WTMM) at the high-frequency range is significantly higher than those observed under external faults. Therefore, extracting WTMM in the range of 3–10 kHz and comparing it with a predefined threshold, is widely used as a typical WT-based protection criterion [29–31]. This threshold (th_{ex}) is determined as follows:

$$|WTMM_{uR1}| > k \times th_{ex} = th_{ex-T} \tag{21}$$

where $WTMM_{uR1}$ is obtained by applying WT to LFVTW at R_1. Also, k is the reliability factor, and $th_{ex\text{-}T}$ is the ultimate protection threshold.

Determining the threshold value has a straight forward procedure. Generally, distinguishing a high-resistance internal fault at the end of the line from a low-resistance forward external fault is the hardest scenario for fault identification. Therefore, *WTMM* of LFVTW under a low-resistance forward external fault is used for adjusting the threshold. This is denoted as f_2 in Fig. 1. To this end, *WTMM* of a 0.1 Ω forward external fault with the waveform presented in Fig. 6 is calculated analytically. Using *db*2 mother wavelet and scale 1 of decomposition, the WTMM for the forward external fault is 50.2, $th_{ex} = 50.2$. By considering a reliability factor of 1.5 to compensate for the impact of noise and measurement errors, the setting threshold in (21) would be thereby $th_{ex-T} = 75.3$.

According to (21) and considering the determined protection threshold, the internal faults can be identified up to a certain resistance. However, beyond that point, the reliability of the method declines. For example, a 350 Ω internal fault at 200 km generates a *WTMM* of 74.8, which is slightly lower than the determined threshold value of 75.2, i.e., it is not recognized by the proposed method. To overcome this challenge and improve protection performance under faults with higher resistances, an improved WT-based protection principle with adaptive threshold setting supported by the analytical approach is proposed in the next subsection.

3.2. Wavelet and decomposition level Selections

The choice of an appropriate mother wavelet is vital for the successful implementation of the proposed WT-based protection method. In this paper, the primary criterion for selection is mainly the ability of different wavelets to improve protection margins under high-resistance internal and low-resistance external faults. To find the most suitable wavelets, a combination of quantitative analysis and trial-and-error methods is employed. In this context, the wavelets db2 and db4 have shown more distinctive results. Note that the proposed protection method is versatile and not dependent on this specific choice, making it adaptable to various wavelet types.

The selection of decomposition level and sampling frequency depend on the frequency content of interest when analyzing the LFVWT. As previously discussed, the high-frequency components of the waveform are typically in the range of 3–10 kHz. Considering the interested frequency range of 5–10 kHz and accounting for low computational burden, a decomposition scale of 1 is preferred for the WT analysis. Hence, a relatively low sampling frequency (20 kHz), is selected for the signal sampling.

3.3. Characteristics of fault-generated traveling waves

The main objective of the proposed method is to distinguish internal faults from reverse and forward external faults. Based on (14), (17), and (18), a backward component of LFVTW (Δu_{b1}) only exists in internal and forward external faults. Therefore, Δu_{b1} can be effectively used to exclude reverse external faults from forward faults. The Δu_{b1} can also be used to classify internal and forward external faults. Fault location, x, and fault resistance, R_f, are the two main factors affecting Δu_{R1} and Δu_{b1} under internal faults (Eq. (14)). On the other hand, based on (17), the two main factors affecting the Δu_{b1} under forward external faults are the size of CLI (L_{CLI}), and fault resistance. Therefore, the effect of Δu_{b1} in the proposed WT-based protection principle can be assessed by analyzing its dependency on fault location, fault resistance, and size of CLI.

1) Impact of Fault Resistance under Internal Faults.

Equations (2)–(4) and (14) quantify the impact of fault resistance under internal faults via $\Delta u_{flt,1}$. According to these terms, higher R_f decreases the magnitude of $\Delta u_{flt,1}$ regardless of the fault type, leading to less severity in the voltage drop magnitude (VDM) of TW. This relation can be corroborated by analyzing Δu_{b1} in the frequency domain as follows:

$$\Delta u_{b1} = \Delta u_{flt,1}.F_e(s) = \begin{cases} \dfrac{\mp\sqrt{2}\,U_{dc}.Z_1}{s(Z_0+Z_1+2R_f)}.F_e(s) & PTG \,/\, NTG \\ \dfrac{-2\sqrt{2}\,U_{dc}.Z_1}{s(2Z_1+R_f)}.F_e(s) & PTP \end{cases} \tag{22}$$

This equation is validated for various cases. As an example, Fig. 10(a) shows the impact of fault resistance on Δu_{b1} in time domain when faults with various resistances happen at 200 km. Therefore, Δu_{b1} is a good indication of VDM under faults and consequently, a good indication of fault resistance.

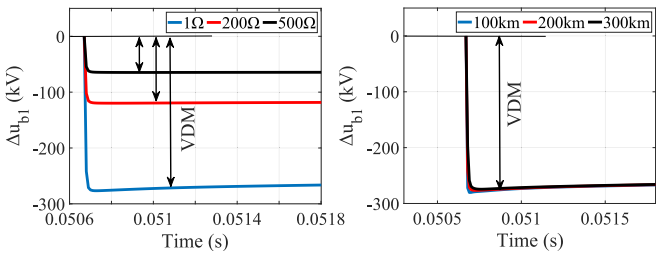

Fig. 10. Impact of: (a) fault resistance; and (b) fault location on Δu_{b1} under internal faults.

2) Impact of Fault Location under Internal Faults.

The impact of fault location on Δu_{b1} is seen through function $F_e(s)$ in (14) and (22). As shown in Fig. 3(a), the magnitude of the line-mode propagation function is ~ 1 over a wide range of frequencies; it is thereby expected to see a low impact of the fault location on Δu_{R1} and Δu_{b1}. This has been confirmed in Fig. 10(b), where the analytical results of Δu_{b1} under internal faults at 100, 200, and 300 km are compared. Since fault location has barely affected the VDM, it can be generally neglected in the design of the proposed protection principle.

3) Impact of Fault Resistance and Size of CLI under Forward External Faults.

Similar to the internal faults, the impact of fault resistance on Δu_{b1} is seen through $\Delta u_{flt,1}$. From (17), VDM would be lower for a larger fault resistance. This can be confirmed by analyzing Δu_{b1} as expressed by (23) and the time-domain analytical results from various forward external faults (Fig. 11(a)).

$$\Delta u_{b1} = \Delta u_{flt,1}.\Lambda_1.F_{el}(s) = \begin{cases} \dfrac{\mp\sqrt{2}\,U_{dc}.Z_1}{s(Z_0+Z_1+2R_f)}.\dfrac{Z_{c1}}{Z_{c1}+sL_{CLI}}.F_{el}(s) & PTG \,/\, NTG \\ \dfrac{-2\sqrt{2}\,U_{dc}.Z_1}{s(2Z_1+R_f)}.\dfrac{Z_{c1}}{Z_{c1}+sL_{CLI}}.F_{el}(s) & PTP \end{cases} \tag{23}$$

The impact of CLI on Δu_{b1} is based on Λ_1 in (23) and can be graphically presented by Fig. 11(b) for a 1 Ω forward external fault. It can be seen that lower CLIs result in a sharper voltage drop rate.

3.4. Improved application of WT with adaptability

Based on the characteristics of Δu_{b1} in terms of fault resistance, R_f, and CLI size an improved WT-based protection is proposed. As displayed in Fig. 10, the fault resistance is the main factor that affects Δu_{b1} under internal faults, i.e., it notably changes VDMs. Therefore, fault resistance can be effectively estimated by VDM. The following expression is used to quantify VDM, where the median of the entire samples of Δu_{b1} within a Δt data window is used.

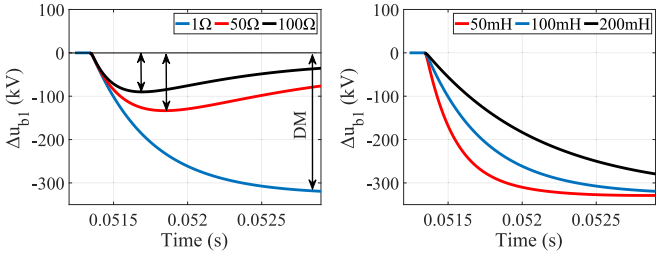

Fig. 11. Impact of: (a) fault resistance; and (b) size of CLI on Δu_{b1} under forward external faults.

$$VDM = \frac{1}{N}\sum_{N}\Delta u_{b1}(n) \tag{24}$$

where N is the number of samples within Δt.

In comparison to the forward-external faults, the response of Δu_{b1} in internal fault cases is square-shaped. This feature can be exploited to classify fault resistance and consequently, adjust the protection threshold. Fig. 12 displays Δu_{b1} under multiple internal and forward external faults with different resistances. The results imply that VDM can be accurately measured using (24) by properly positioning Δt after the fault inception for internal faults. This VDM, which is mainly affected by the fault resistance, can be precisely quantified, independent of the position of Δt. However, when the position of Δt shifts in time, VDM cannot be accurately determined under forward external faults due to the decaying shape of the LFVTW (Fig. 12). Moreover, the analytical study in Fig. 12 shows that VDMs under forward external faults is lower than those under internal faults when fault resistances are identical. According to Fig. 11(b), larger CLI sizes also cause the waveforms to have smoother shapes, and consequently, they lower the magnitude of the calculated VDMs inside the data window. Therefore, VDM is a good criterion for classifying the quantity of fault resistance under internal and forward external faults and adjusting the protection threshold.

On the other hand, VDM is close to zero under reverse external faults, as Δu_{b1} does not exist in these scenarios (Eq. (18)). Hence, VDM not only can be used to estimate the fault resistance and re-adjust the threshold setting, it can also be used to exclude reverse external faults from forward faults.

To demonstrate the process of the proposed protection method, first, Δu_{R1} and Δu_{b1} under a set of SPG internal and forward external faults with various resistances are analytically calculated. Then, the resulting WTMMs and VDMs are calculated, which are presented in Table 2. Since fault location has negligible impact, it is considered fixed at 200 km of the 400-km transmission line. The mother wavelet is *db*2, and the sampling frequency is 20 kHz. The selection of Δt is derived from the analytical studies in Subsection 3.3, calculated two samples after fault signature arrival time (FSAT).

The presented approach can be explained by an example, wherein a PTG internal fault at 300 km with $R_f = 500\ \Omega$ is simulated. By using (24), VDM = -63.3 kV. Since VDM is significant, the fault is classified as the forward one (either internal or forward external). Based on Table 2, when the fault is internal, R_f should be in the range of 400–700 Ω, while it lies within the 100–200 Ω range for forward external faults. Therefore, an estimation of fault resistance is available and the threshold in (21) can be adjusted accordingly. As a result, there is no need to regulate the threshold based on the WTMM of the low-resistance forward external fault, i.e., 0.1 Ω forward external fault in Table 2(50.2). Hereby, the threshold can be set at lower levels; thus, internal faults with higher resistance can be distinguished from external faults. In other words, the new threshold can be adjusted in the range of 13.5–25.9, corresponding to the fault resistance range of 100–200 Ω. Therefore, the th_{ex} in (18), is set to the new value $\sim(13.5 + 25.9)/2 = 19.7$, and the final threshold value is $th_{ex\text{-}T} = 1.5 \times 19.7 = 29.6$. Since the WTMM of the 500 Ω fault is 56.2, it can be effectively identified as an internal fault with the new threshold, which was not possible based on the old threshold of 75.3.

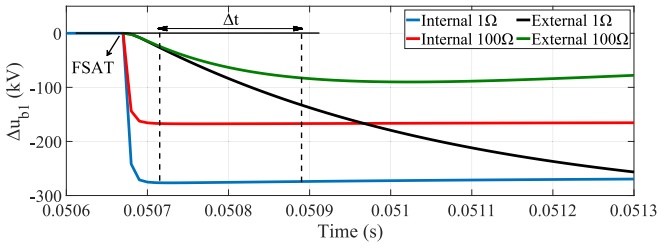

Fig. 12. Position of Δt after FSAT and comparison of Δu_{b1} under internal and forward external faults with similar resistances.

Table 2
Absolute WTMM and VDM under various SPG faults.

Internal faults			Forward external faults		
R_f (Ω)	*VDM* (kV)	|*WTMM*|	R_f (Ω)	*VDM* (kV)	|*WTMM*|
1	−272.4	250.9	0.1	−150.4	50.2
25	−235.5	216	25	−127.5	41.5
50	−206.3	188.7	50	−109.2	35.5
100	−165.4	150.5	100	−82.8	25.9
200	−118.3	107.2	200	−53	13.5
400	−75.3	68	300	−37.8	6.6
700	−48.7	43.9			
1000	−35.9	32.4			

Table 3
Absolute WTMM and VDM under various PTP faults.

Internal faults			Forward external faults		
R_f (Ω)	*VDM* (kV)	|*WTMM*|	R_f (Ω)	*VDM* (kV)	|*WTMM*|
1	−695.4	622.1	0.1	−257.2	123
25	−632.4	565.6	25	−239.8	116.7
50	−577.9	516.7	50	−223.5	112.4
100	−492.9	440.6	100	−195.5	104.4
200	−380.8	340.3	200	−154.4	90.5
400	−261.7	233.8	300	−125.7	79.3
700	−178	159.1			
1000	−134.8	120.6			

Based on the described procedure, the adaptive threshold adjustment is integrated into the proposed WT-based protection principle. It is worth noting that a similar procedure is exploited for PTP faults, using the analytically computed data provided in Table 3.

4. Proposed wavelet transform-based protection principle

Fig. 13 shows the flowchart diagram of the proposed protection principle. An under-voltage criterion is considered as a start-up unit (SU) as defined in (25) to discriminate between faulted and normal conditions:

$$\Delta u_{R1} < -th_{su} \tag{25}$$

where th_{su} is the threshold that is set as $0.05U_{dc}$ in this paper, e.g., 25 kV for a 500 kV system. The time instant at which (25) is satisfied is denoted by n_0. After the algorithm's initiation, a direction criterion (DIR) is used to exclude reverse external faults. As discussed in the previous section, Δu_{R1} is close to zero under reverse external faults. Therefore, a median of Δu_{R1} over a data window of five samples is used. This data window, which is identical to (24), can be expressed as follows:

$$VDM = \frac{1}{5}\sum_{n=n_0+1}^{n_0+5}\Delta u_{b1}(n) < th_{dir} \tag{26}$$

The direction threshold value in the recent equation (th_{dir}) is defined in such a way that high-resistance forward faults can be effectively recognized. Based on Tables 2 and 3, the high-resistance internal and forward external faults have VDMs of −35.9 kV and −37.8 kV under SPG faults and −134.8 kV and −125.7 kV under PTP faults, respectively. Therefore, th_{dir} is −35 kV and −125 kV for SPG and PTP forward faults, respectively.

After the exclusion of reverse faults, the next step is to identify the faulty pole. According to (22) and Tables 2 and 3, VDMs under PTP faults are more severe than those under SPG faults; thus, the computed *WTMMs* vary significantly. Therefore, the faulty pole should be identified before adjusting the threshold value of the WT-based protection unit (WTPU). As expressed by (2)–(4), the zero-mode voltage component is negative, positive, and zero for PTG, NPG, and PTP faults, respectively. Thus, the zero-mode voltage component can be used as a fault pole

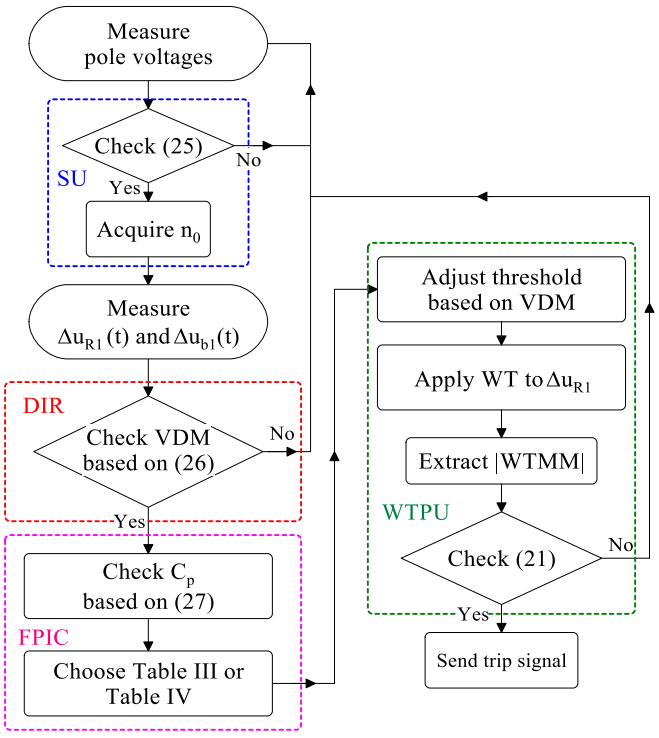

Fig. 13. Schematic diagram of proposed protection algorithm.

identification criterion (FPIU) with:

$$C_p = \frac{1}{5}\sum_{i=n_0+1}^{n_0+5} u_0(i) \tag{27}$$

where u_0 is the zero-mode voltage component at the location R_1. The threshold in (27) is determined in a way that the faulty pole can be reliably identified under high-resistance internal and external faults. Hence, the protective threshold is as indicated in (28), and its threshold (th_p) is set to 35 kV:

$$\begin{cases} C_p < -th_p & PTG \\ -th_p < C_p < th_p & PTP \\ C_p > th_p & NTG \end{cases} \tag{28}$$

When the faulty pole is discovered, either Table 2 for SPG faults or Table 3 for PTP faults is chosen for threshold adjustment. The threshold adjustment is performed using the forward external data of Tables 2 and 3. Afterward, the WT is applied on Δu_{R1} to extract the *WTMM* of $d_1(k)$ (taken from (17)); hence, it is determined that the forward fault is internal or external. In internal fault cases, a trip signal is issued.

5. Simulation study

The performance of the proposed protection principle is assessed in the four-terminal MMC-based HVDC grid, explained in Section 2, simulated in PSCAD/EMTDC. Fault scenarios, initiating at $t = 50$ ms, are also illustrated in Fig. 1. The transmission lines are modeled using frequency-dependent parameters. Considering a 20 kHz sampling frequency, $\Delta t = 0.25$ ms. Wavelet transform at scale 1 over $\Delta t_w = 1$ ms is employed to extract WTMM. Due to simplicity of SU, its performance will not be discussed in this paper. Since the characteristic of PTG and NTG faults is very similar, the PTG fault scenarios are solely evaluated.

5.1. Internal and external faults

Table 4 presents a set of various internal fault scenarios with different locations and resistances. To evaluate the information

Table 4
Performance of proposed protection method under various internal fault scenarios.

Fault Type	x (km)	R_f (Ω)	VDM (kV)	C_p (kV)	|WTMM|	Old th_{ex-T}	New th_{ex-T}
PTG	50	10	−260.2	−505.8	242.1	75.3	75.3
		150	−139.6	−272	128.4		69.3
		750	−46.6	−91.9	42.6		15.9
	150	35	−233.6	−410.2	200.8	75.3	75.3
		425	−72.5	−133.9	64.4		32.4
		700	−49	−91.1	43.6		17.5
	250	75	−183	−231.9	159.4	75.3	75.3
		225	−110.2	−139.7	95.5		54.2
		600	−55.1	−87.9	47.7		21.6
	350	1	−269.9	−256.9	245	75.3	75.3
		500	−63.2	−59.8	54.1		26.6
		850	−41.3	−54.3	35.1		12.3
PTP	100	700	−179.1	−0.8	153.9	184.5	148.3
	200		−176.4	−1.4	157.2		146.9
	300		−174.4	−1.3	155.5		145.8

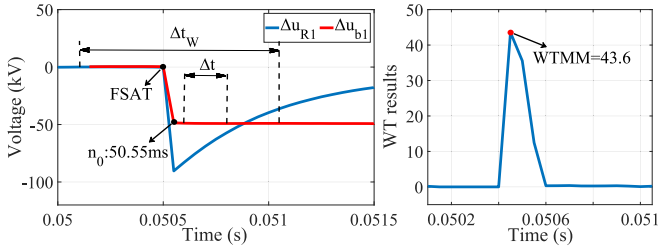

Fig. 14. 700 Ω PTG fault at 150 km: (a) Δu_{R1} and Δu_{b1}; (b) WT results.

provided in Table 4, the 700 Ω fault at 150 km is considered, while its Δu_{R1}, Δu_{b1} and WT results are shown in Fig. 14.

It is seen from the results that after SU satisfaction at $n_0 = 50.55$ ms, the algorithm immediately starts measuring Δu_{b1} to check the direction criterion of (26) over Δt. Since VDM = −49 kV, the fault is identified as forward, and the process of R_f classification begins. To this end, C_p is calculated as −91.1 kV from (27). Further, since the fault is a PTG type, the threshold is adjusted using Table 2. According to the forward external faults of Table 2 and the VDM levels, the threshold should be set within the 6.6–15.3 range, which can be obtained via interpolation in the ranged. Based on (21), the threshold is adaptively re-tunned at $th_{ex-T} = 1.5 \times 11.7 = 17.5$. Then, WT is applied and the results are as shown in Fig. 14 (b). It is readily seen that *WTMM* = 43.6. Note that, this fault would be recognized as external for the old threshold setting, i.e., 75.3. However, using the new adjusted threshold, 17.5, it is accurately identified as internal.

As an example for PTP faults, a 700 Ω internal fault at 300 km is simulated. The simulation outputs, including Δu_{R1}, Δu_{b1}, and WT results

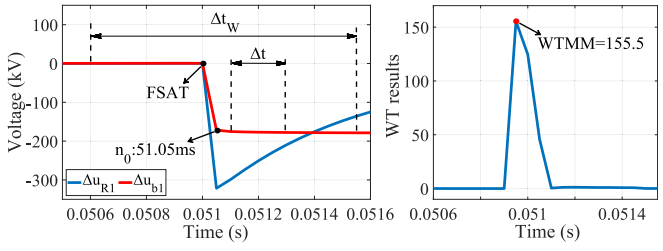

Fig. 15. 700-Ω PTP fault at 300 km for: (a) Δu_{R1} and Δu_{b1}; and (b) WT results.

Table 5
Performance of proposed protection method under various external fault scenarios.

Fault Type	x (km)	R_f (Ω)	*VDM* (kV)	C_p (kV)	|*WTMM*|	Old th_{ex-T}	New th_{ex-T}
PTG	f_2	0.1	−149.6	−93.8	49.6	75.3	74.9
		25	−126.9	−83.4	41.3		62
	f_3	0.1	0.47	–	–	75.3	–
		25	0.57	–	–		–
	f_4	0.1	−35.6	−41.1	5.9	75.3	9.9
	f_5	0.1	0.35	–	–	75.3	–
PTP	f_2	0.1	−256.2	−0.5	123.5	184.5	181.1
	f_3	0.1	1.05	–	–	184.5	–

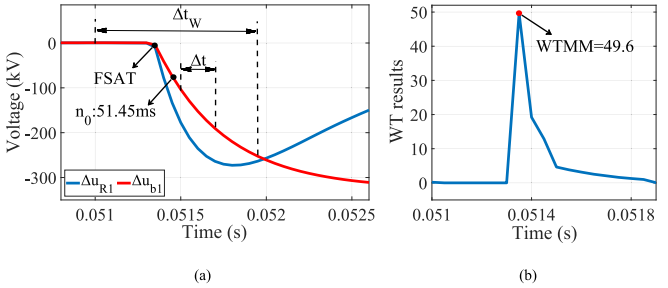

Fig. 16. 0.1-Ω PTG forward external fault: a) Δu_{R1} and Δu_{b1}; (b) WT results.

are shown in Fig. 15. The VDM and C_p are −174.4 kV and −1.3 kV, respectively; the fault is accordingly classified as a forward PTP fault. Therefore, the threshold is re-adjusted from the range 90.5 to 104.4 based on VDM level and Table 3. Similar to previous case, after performing interpolation within this range, $th_{ex-T} = 1.5 \times 97.2 = 145.8$. After applying the WT, *WTMM* is determined as 155.5. It can be seen that based on the old threshold, 184.5, this fault is identified as external. However, with the new threshold, the it is correctly identified as internal.

The explained procedure is performed for numerous fault scenarios including the cases in Table 4. Therefore, the proposed protection principle is reliable under all internal faults up to 850 Ω and 700 Ω for SPG and PTP faults, respectively.

The performance of the proposed method is also examined under reverse and forward external faults, detailed in Table 5. A 0.1 Ω forward external fault at f_2 is simulated. The results as shown in Fig. 16 (a) and (b).

The same process is used to adjust the threshold. The VDM and C_p are −150.4 kV and −93.8 kV, respectively. Hence, the fault is categorized as PTP, either internal or forward external. Based on Table 3, the range of modified threshold is 41.5–50.2. After employing the WT, a *WTMM* of 49.6 is obtained. This case is thereby recognized as a forward external fault as $th_{ex-T} = 1.5 \times 49.9 = 74.9$.

It is concluded from the presented analysis that the proposed protection method effectively identifies all types of internal and external faults, for a wide range of fault resistances at different locations. This promising performance is achieved through adaptive threshold determination.

5.2. Impact of noise disturbance

Noise disturbance is an important variable that can affect the effectiveness of the protection methods. In this regard, numerous fault scenarios are simulated under noise disturbance (Table 6). As an example, a 400 Ω PTG fault at 200 km is considered when a white Gaussian noise with a 35 dB signal-to-noise ratio is applied to the voltage measurements. The results Δu_{R1} and Δu_{b1} with and without the additive noise are

Table 6
Performance of proposed protection method under noisy measurements.

	Fault Resistance (Ω)	VDM (kV)	|WTMM|	Old th_{ex-T}	New th_{ex-T}
Without noise	400	−75.5	66.9	75.3	34.3
With noise		−77.5	51.7		35.5
Without noise	850	−42.3	35.9	75.3	13
With noise		−40.8	33.1		11.9

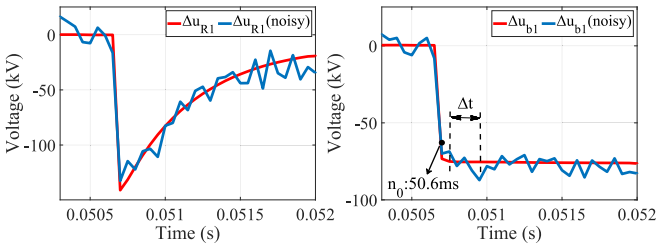

Fig. 17. Δu_{R1} and Δu_{b1} under: (a) no noise; and (b) 35 db noisy measurements.

depicted in Fig. 17 (a) and (b), respectively. According to Table 6, the calculated VDMs, with and without the noise disturbance, are very close, i.e., −77.5 kV and −75.5 kV, respectively. This insignificant impact of noise on VDM is due to the square shape response of Δu_{b1} and exploiting this feature via the definition of (26), measuring the median of the wave over Δt. Hence, since VDM is accurately measured in the noise presence, the precise adjustment of the threshold can be performed accordingly, which translates into improved overall performance of the proposed protection principle.

This has been endorsed in Table 6 where the 400 Ω fault cannot be discovered with the old threshold. However, it is reliably identified after the threshold adjustment.

Overall, the proposed protection principle has solid performance under noise disturbance up to resistance of 850 Ω.

5.3. Impact of sampling frequency

In this paper, the frequency range of interest for WTMM extraction is 5–10 kHz. Based on this range and the context of WT, a sampling frequency of 20 kHz has been selected. When a sampling frequency greater than 20 kHz is set, a higher decomposition level is required for the WTMM extraction. This degrades the speed of the proposed protection method as the computational burden increases. Therefore, the investigations are focused on a 10 kHz sampling frequency exploitation to meet the frequency range requirements and avoid increasing the decomposition level.

After determining the VDMs and *WTMMs* for the 10 kHz sampling frequency, table data similar to Tables 2 and 3 are obtained for this sampling frequency. As an example, the performance of the proposed method for a specific case, an internal fault at 300 km with resistance of 850 Ω, is presented in Table 7. It is evident that this fault sampled at 10 kHz is not detectable, as its |*WTMM*| (34) barely reaches the new threshold (39.9). The new adjusted threshold, 39.9 for the 10 kHz sampling frequency is noticeably higher than the 20 kHz threshold,

Table 7
Performance of the proposed protection method with 10 kHz sampling frequency.

Sampling frequency (kHz)	VDM (kV)	C_p (kV)	|WTMM|	Old th_{ex-T}	New th_{ex-T}
20	−41.4	−60.8	36.4	75.3	12.4
10	−41.5	−47.5	34	106.1	39.9

Table 8
Performance of proposed protection method under different cli sizes.

Fault Type	*CLI* (mH)	Fault Resistance (Ω)	*VDM* (kV)	C_p (kV)	$\lvert WTMM \rvert$	Old th_{ex-T}	New th_{ex-T}
PTG	**25**	300	−83.7	−73	73.1	183.1	72.7
	50	500	−64.3	−69.2	53.3	142.4	48.8

12.4. Hence, this fault is missed by the proposed protection method.

According to the thorough analysis conducted with the 10 kHz sampling frequency, the proposed protection method is reliable for the entire length of the transmission line up to 750 Ω. This lower sensitivity compared to the 20 kHz case (850 Ω) is mainly due to the shift in the frequency range of interest, which reduces the performance when adjusting the threshold. Even though the performance degrades to some extent, 750 Ω is still a solid performance with 10KHz sampling frequency.

5.4. Impact of CLI size

The impact of *CLI* on the performance of the proposed method is assessed in this subsection. Typically, a smaller CLI poses more challenges for protection principles, as the impact of line boundary diminishes, making it more difficult to distinguish internal and external faults. Similar to previous studies, VDM and $|WTMM|$ are computed for smaller CLIs, e.g., 25 and 50 mH. The remainder of the performance evaluation process is similar to the methodology presented in Section V-A for internal and external faults. Table 8 presents a few results for internal high-resistance faults, simulated at 300 km.

It can be concluded that the maximum detectable fault resistances for PTG faults with $CLI = 25$ and 50 mH are ∼ 300 and ∼ 500 Ω, respectively. Accordingly, it can be deduced that the presented method has high degree of reliability, sensitivity, and selectivity, even when the system's *CLI* is as low as 25 mH. Overall, robust analytical calculation of LFVTW and adjustment of protective threshold are the essential factors in the enhanced performance of the proposed protection method.

5.5. Protection response time

The response time of the proposed protection method can be demonstrated using Fig. 14, Fig. 15 or Fig. 16. The two primary variables that determine the total response time are: length of the data windows (Δt_{dw}), and the collective computational processing time of all protection units (Δt_{com}). The total delay time (Δt_T) can be presented as follows:

$$\Delta t_T = \Delta t_{dw} + \Delta t_{com} \tag{29}$$

In the proposed algorithm, the data window (Δt) used for SU, DIR, and FPIU determination is the same, consisting of five samples from $n_0 + 1$ to $n_0 + 5$. The data window for WT analysis is Δt_w with 20 samples, from n_0–9 to $n_0 + 10$. According to Figs. 14, 15, and 16, the relevant portion of the data window, affecting the response time accounts for half of the Δt_{dw}. This data window starts from n_0 to $n_0 + 10$, corresponding to ∼ 0.5 ms. Thus, $\Delta t_{dw} = 0.5$ ms.

On the other hand, the proposed algorithm sequentially applies Eqs. (21) and (25)–(27) for various protective purposes. Therefore, the computational time for each step should also be reflected in Δt_{com}. The computational time for Eqs. (25)–(27) involves executing straightforward mathematical calculations and can be neglected. However, the process of extracting the *WTMM* using WT imposes some time delay. Given that the decomposition level is 1, this computational delay is lower than the cases with higher decomposition levels, taking around 0.05 ms to complete. Thus, Δt_{com} would be smaller than 0.1 ms. Finally, considering other delay factors, e.g., sensor detection time, the total delay time, Δt_T, is generally lower than 1 ms.

5.6. Comparison to existing methods

The overall performance of the proposed method is demonstrated through an in-depth comparison over existing WT-based protection methods [26–33]. The comparative results are presented in Table 9. It should be noted that the protection action time in Table 9 measures the duration from observing the LFVTW of a fault at the DC terminal to the protection relay outputting a trip signal.

- Enhanced sensitivity and selectivity: The most prominent features of the proposed protection method are the enhanced sensitivity and selectivity in distinguishing internal faults from external faults, even when the fault resistances reach up to 850 Ω. This clearly outperforms the works in [28–33], where sensitivity is limited to around 300–400 Ω. While studies in [26] and [27] exhibit improved fault detection up to 500–600 Ω, they have less robustness against noise disturbance. They also require higher sampling frequencies (50–100 kHz) compared to the proposed method, which operates reliably at 10 and 20 kHz. Furthermore, the proposed protection method maintains strong performance even at low *CLI* levels of 25 mH, whereas [27] requires $CLI \geq 50$ mH. Moreover, various wavelets and decomposition levels are used for different relays at different DC terminals of the system in [28], which makes the determination of a unified protection approach difficult.
- Robustness to noise: Improved performance under noise disturbance is another strong aspect of the proposed protection method. In similar studies, namely [29,31] and [33], good performance under noise is observed. The reasons, aside from utilizing the WT inherent noise-filtering capability, are proper selection of mother wavelet (sym8 in [29]) or using higher decomposition levels (fourth level). However, in the proposed protection method, aside from the filtering

Table 9
Comparison to similar WT-based methods.

Reference number	Protection action time	Sampling frequency	Fault resistance robustness	Robustness to noise	Accuracy in analytical calculation
26	<1 ms	100 kHz	<500 Ω	low	medium
27	>1 ms	≥50 kHz	∼600 Ω	low	low
28	∼3 ms	100 kHz	∼300 Ω	–	low
29	∼2.2 ms	20 kHz	∼200 Ω	medium	low
30	>2 ms	10 kHZ	∼300 Ω	–	medium
31	–	500 kHz	∼400 Ω	medium	medium
32	∼1.2 ms	1 MHz	∼300 Ω	–	low
33	<1 ms	10 kHz	∼300 Ω	medium	low
Proposed method	<1 ms	10 kHz	850 Ω	high	high

capability of WT, employing a robust approach in defining the fault resistance classification is another major enhancement criterion in noise impact mitigation. This insignificant impact of noise on VDM is due to two key design factors. First in the definition of (26) in measuring the median of the wave over Δt, which effectively mitigates the impact of noise. Second, in the context of the waveform used for fault detection analysis. When analyzing internal faults, Δu_{R1} exhibits sharp temporal variations (as seen in Fig. 4 or Figs. 14 and 15). However, by focusing on the backward wave (Δu_{b1}) and using (26), the fault resistance classification and subsequent threshold adjustment become more robust to noise interference. On the other hand, this process during external faults is also relatively strong for dealing with noise, as CLI size prevents severe variations in Δu_{b1} and hence, mitigates the detrimental impact of noise disturbance. Given that threshold adjustment is a significant part of the proposed protection method, the noise-resilient fault resistance classification and the consequent threshold adjustment significantly enhance the overall performance, especially under noisy conditions. Overall, better noise-handling performance compared to [29,31] and [33] is achieved.

- Improved adaptability: threshold determination process is a challenging task for protection principles especially, for WT-based solutions as discussed in [37]. Therefore, accurate modeling of system behavior, with specific focus on the modeling of wave impedances and propagation functions have significant importance. In this study, these factors are carefully considered, making the proposed protection method more reliable than its counterparts, many of which require enhancements in their analytical calculations. References [26,30], and [31] stand out for their more accurate analytical calculations of fault-generated waveforms compared to other studies in Table 9. However, these methods still have shortcomings compared to the proposed protection method. For instance, waveform analysis under external faults and consideration for the zero- and line-mode components are absent in [26]. In comparison to [26], both references [30] and [31] provide improved analytical studies for both internal and external faults. However, the simplifications in modeling the wave impedances and propagation function, without using a more accurate VF technique, make these protection methods susceptible to some degree of error. This level of error and its negative impact of the WT-based protection methods are discussed in subsection 2.4.

6. Conclusion

In this paper, a novel WT-based protection principle is proposed for MMC-based HVDC grids, exploiting an adaptive threshold setting. To this end, the improved analytical expression of LFVTW under internal and external faults is initially derived. Then, based on the analytical evaluations, it is discussed that VDM of the backward component of LFVTW is a suitable criterion to estimate the fault resistance and classify faults. When an estimation of fault resistance is available, it can be used to adjust the protective threshold setting and improve the performance of WT-based protection methods. Therefore, the analytical approach presents an essential role not only as a robust procedure to analyze TWs under fault conditions but also as an accurate method for threshold adjustment. Since WTMM is used as the fault detection criterion, the accuracy of LFVTW modeling is improved to avoid unnecessary calculation errors, which can affect the WT-based protection principles. This subject is properly discussed in this paper, which is another strong point of this research study compared to similar studies. The simulation results confirmed that the proposed protection principle can enhance the application of WT in fault identification up to 850 Ω and 700 Ω for SPG and PTP faults, respectively. Moreover, the robustness of the proposed protection principle using a low sampling frequency of 10 kHz, under low CLI size (25mH) and high noise disturbance (35 dB SNR) is confirmed. Given the complexity of future HVDC grid topologies, it is worth investigating the combination of WT-based protections with machine learning approaches to enhance fault classification performance, which can be covered in future studies.

CRediT authorship contribution statement

Farzad Dehghan Marvasti: Writing – review & editing, Writing – original draft, Validation, Methodology, Investigation, Formal analysis. **Ahmad Mirzaei:** Writing – review & editing, Supervision, Methodology, Conceptualization. **Reza Bakhshi-Jafarabadi:** Writing – review & editing, Writing – original draft, Supervision. **Marjan Popov:** Writing – review & editing, Supervision.

Declaration of competing interest

The authors declare that they have no known competing financial interests or personal relationships that could have appeared to influence the work reported in this paper.

Data availability

No data was used for the research described in the article.

References

[1] Kim CK, Sood VK, Jang GS, Lim SJ, Lee SJ. HVDC transmission: power conversion applications in power systems. John Wiley & Sons (Asia) 2009.

[2] Bellmunt OG, Ferre AJ, Sumper A, Jane JB. Control of a wind farm based on synchronous generators with a central HVDC-VSC converter. IEEE Trans Power Syst 2011;26(3):1632–40.

[3] Wang Y, Wen W, Zhang C, Chen Z, Wang C. Reactor sizing criterion for the continuous operation of meshed HB-MMC-based MTDC system under DC faults. IEEE Trans Ind Appl 2018;54(5):5408–16.

[4] A. Li, Z. Cai, Q. Sun, X. Li, D. Ren, and Z. Yang, "Study on the dynamic performance characteristics of HVDC control and protections for the HVDC line faults," *Proc. Power Energy Soc. Gen. Meeting*, Calgary, AB, 2009, pp. 1-5.

[5] Leterme W, Beerten J, Van Hertem D. Nonunit protection of HVDC grids with inductive DC cable termination. IEEE Trans Power Del 2016;vol. 31, no. 2.

[6] F. D. Marvasti, A. Mirzaei, M. Savaghebi and M. R. Jannesar, "A Pilot protection scheme for HVDC transmission lines based on simultaneous existence of forward and backward voltage travelling waves," *2022 IEEE 13th International Symposium on Power Electronics for Distributed Generation Systems (PEDG)*, Kiel, Germany, 2022, pp. 1-6.

[7] Li C, Gole A, Zha C. A fast DC fault detection method using DC reactor voltages in HVdc grids. IEEE Trans Power Del 2018;33, no. 5.

[8] Li S, Chen W, Yin X, Chen D, Teng Y. A novel integrated protection for VSC-HVDC transmission line based on current limiting reactor power. IEEE Trans Power Del 2020;35(1):226–33.

[9] Liu J, Tai N, Fan C. Transient-voltage-based protection scheme for DC line faults in the multiterminal VSC-HVDC system. IEEE Trans Power Del 2017;32(3):1483–94.

[10] Sneath J, Rajapakse AD. Fault detection and interruption in an earthed HVDC grid using ROCOV and hybrid DC breakers. IEEE Trans Power Del 2016;31(3):973–81.

[11] X. Yu, J. Gu, X. Zhang, J. Mao and L. Xiao, "A non-unit transmission line protection scheme for MMC-HVDC grids based on a novel distance criterion," *Int J Electr Power Energy Syst*, vol. 151, no. 109151, 2023.

[12] Y. Qin, M. Wen, X. Yin, Y. Bai and Z. Fang, "A novel distance protection for MMC-HVDC lines based on the equivalent capacitance voltage," *Int J Electr Power Energy Syst*, vol. 137, no. 107850, 2022.

[13] Zhang C, Song G, Meliopoulos APS, Dong X. Setting-less nonunit protection method for DC line faults in VSC-MTdc systems. IEEE Trans Ind Electron 2022;69(1): 495–505.

[14] Zhang C, Song G, Dong X. Non-unit ultra-high-speed DC line protection method for HVDC grids using first peak time of voltage. IEEE Trans Power Del 2021;36(3): 1683–93.

[15] Saleh KA, Hooshyar A, El-Saadany EF, Zeineldin HH. Protection of high-voltage DC grids using traveling-wave frequency characteristics. IEEE Syst J 2020;14(3): 4284–95.

[16] Lan T, Li Y, Duan X. High fault-resistance tolerable traveling wave protection for multi-terminal VSC-HVDC. IEEE Trans Power Del 2021;36(2):943–56.

[17] Li B, Lv M, Li B, Xue S, Wen W. Research on an improved protection principle based on differential voltage traveling wave for VSC-HVDC transmission lines. IEEE *Trans Power Del* 2020;35(5):2319–28.

[18] Zhang C, Song G, Wang T, Dong X. An improved non-unit traveling wave protection method with adaptive threshold value and its application in HVDC grids. IEEE Trans Power Del 2020;35(4):1800–11.

[19] Chu X. Transient numerical calculation and differential protection algorithm for HVDC transmission lines based on a frequency-dependent parameter model. Int J Electr Power Energy Syst 2019;108:107–16.

[20] S. Xue, J. Lu, Y. Sun, S. Wang, B. Li, and B. Li, "A reverse travelling wave differential protection scheme for DC lines in MMC–HVDC system with metallic return," *Int J Electr Power Energy Syst*, vol. 135, no. 107521, 2022.
[21] Lan T, Xiao H, Li Y, Chen J. Enhanced current differential protection for HVDC grid based on Bergeron model: a parameter error tolerable solution. IEEE Trans Power Del 2021;36(3):1869–81.
[22] Yu X, Xiao L. A DC fault protection scheme for MMC-HVDC grids using new directional criterion. IEEE Trans on Power Del 2021;36(1):441–51.
[23] Li B, Li Y, He J, Li B, Liu S, b. Liu,, et al. An improved transient traveling-wave based direction criterion for multi-terminal HVDC grid. IEEE Trans Power Del 2020;vol. 35, no. 5.
[24] Z. Li, Y. Ye, N. Tong, X. Lin, C. Li, N. Jin, et al. "High error-tolerable unit protection for VSCMTDC independent of data synchronization," *Int J Electr Power Energy Syst*, vol. 124, no. 106393, 2021.
[25] N. Tong, X. Lin, C. Li, Q. Sui, L. Chen, Z. Wang, et al. "Permissive pilot protection adaptive to DC fault interruption for VSC-MTDC," *Int J Electr Power Energy Syst*, vol. 123, no. 106234, 2021.
[26] Psaras V, Tzelepis D, Vozikis D, Adam GP, Burt G. Non-unit protection for HVDC grids: an analytical approach for wavelet transform-based schemes. IEEE Trans Power Del 2021;36(5):2634–45.
[27] Lan T, Xiao H, Li Y, Chen J. Computationally effective frequency transient-based transmission line protection for multiterminal VSC-HVdc. IEEE Trans Industr Inform 2022;18(9):5925–35.
[28] Zou G, Feng Q, Huang Q, Sun C, Gao H. A fast protection scheme for VSC based multi-terminal DC grid. Int J Electr Power Energy Syst 2018;98:307–14.
[29] Xiang W, Yang S, Xu L, Zhang J, Lin W, Wen J. A transient voltage-based DC fault line protection scheme for MMC-based DC grid embedding DC breakers. IEEE Tran Power Del 2019;34(1):334–45.
[30] Li B, Li Y, He J, Wen W. A novel single-ended transient-voltage-based protection strategy for flexible DC grid. IEEE Tran Power Del 2019;34(5):1925–37.
[31] Pei X, Pang H, Li Y, Chen L, Ding X, Tang G. A novel ultra-high-speed traveling-wave protection principle for VSC-based DC grids. IEEE Access 2019;7:119765–73.
[32] Tang L, Dong X, Shi S, Y, Qui,. A high-speed protection scheme for the DC transmission line of a MMC-HVDC grid. Elect Power Syst Research 2019;168:81–91.
[33] Sabug L, Musa A, Costa F, Monti A. Real-time boundary wavelet transform-based DC fault protection system for MTDC grids. Int J Electr Power Energy Syst 2020;115.
[34] CIGRE Working Group B4.57, *Guide for the Development of Models for HVDC Converters in a HVDC Grid*, CIGRE Technical Brochure, no. 604, 2014.
[35] Suonan J, Gao S, Song G, Jiao Z, Kang X. A novel fault-location method for HVDC transmission lines. IEEE Trans Power Del 2010;25(2):1203–9.
[36] *EMTDC User Guide, Transient analysis for PSCAD power system simulation*. v4.6, Manitoba HVDC research Centre, 211 Commerce Drive, Manitoba, Canada, 2016.
[37] Costa FB. Fault-induced transient detection based on real-time analysis of the wavelet coefficient energy. IEEE Trans Power Del 2014;29(1):140–53.